Progress In Electromagnetics Research, Vol. 170, 1–15, 2021

Designing Nanoinclusions for Quantum Sensing Based on Electromagnetic Scattering Formalism

Constantinos Valagiannopoulos*

(*Invited Paper*)

Abstract—Quantum interactions between a single particle and nanoinclusions of spherical or cylindrical shape are optimized to produce scattering lineshapes of high selectivity with respect to impinging energies, excitation directions, and cavity sizes. The optimization uses a rigorous solution derived via electromagnetic scattering formalism while the adopted scheme rejects boundary extrema corresponding to resonances that occur outside of the permissible parametric domains. The reported effects may inspire experimental efforts towards designing quantum sensing systems employed in applications spanning from quantum switching and filtering to single-photon detection and quantum memory.

1. INTRODUCTION

Quantum mechanics are present in every aspect of the physical world, including the measuring devices whose accuracy is limited due to the inherent uncertainty in the position and the velocity of quantum particles. To remedy such a weakness in metrology, techniques like squeezing coherent states or quantum entanglement have been adopted, in an attempt to enhance the measurement reliability [1]. The key process behind any similar attempt is the quantum sensing, a rapidly growing and well-funded branch of research [2] that delivers revolutionary experimental setups like nitrogen-vacancy centers in diamond with unlimited photostability [3]. In addition, quantum sensing precision can be amplified with use of memories able to enhance the time interval over which wave function phase can be accumulated [4] or via quantum illumination assisted by highly efficient microwave-optical converters that mitigate defects in generating microwave entanglement [5]. Finally, methodologies based on coherent quantum interpolation have been developed to lift the hardware restrictions that hinder the sensor performance [6] while adapting the spin readout basis in real time can lead to interferometric sensitivity that surpasses standard measurement limits [7].

Given the similarity of the governing dynamic laws (Helmholtz vs Schrödinger equations) and the accompanying boundary conditions imposed to the electromagnetic fields or the wave functions of quantum particles, a clear analogy between electrodynamics and quantum mechanics is identified. Therefore, the design of quantum sensing components has been greatly aided by methods developed for electromagnetic waves like the transfer matrix approach implemented at several quantum interfaces [8]. Importantly, the quantum analogues of electrodynamic metamaterials have been thoroughly investigated [9, 10] while the interference within a Fabry-Perot cavity has been extensively examined from the matter-wave point of view [11] and has given highly selective responses with respect to incidence direction [12] and impinging energy [13]. Moreover, multiple quantum barriers with high sensing capability are analytically solved with techniques employed in treating the electromagnetic

Received 23 November 2020, Accepted 5 January 2021, Scheduled 14 January 2021

* Corresponding author: Constantinos Valagiannopoulos (konstantinos.valagiannopoulos@nu.edu.kz).

The author is with the Department of Physics, Nazarbayev University, Qabanbay Batyr Ave 53, Nur-Sultan, KZ 010000, Kazakhstan.

interactions between consecutive slabs [14] while a similar setup is utilized to guess the effective quantum features of a planar sample from transmissive measurements [15].

Typical configurations that serve various sensing purposes require the development of nanometer-sized inclusions into a suitable host; such a fabrication is feasible with a variety of approaches. In particular, semiconducting nanowires can be engraved into specific backgrounds via chemical bottom-up methods to encode high resolution morphology [16] while physical epitaxial techniques have been utilized for the same purpose [17]. Importantly, top-down fabrication methods for creating diamond nanowires in polycrystalline diamond that allow for significant collection efficiency of emitted photons, are largely employed for quantum sensing and information processing applications [18]. Another common inclusion shape is the spherical one and can be also successfully synthesized via an one-step route in nanometer dimensions with controllable shell thickness [19] or even by self-assembly processes producing accurately controlled geometrical conformations [20]. It is also remarked that core-shell nanospheres can be prepared by solution-based template wetting method [21], where the tension between different materials shapes the required nanocavities.

The topic of this study is the interaction of matter waves with related nanoinclusions by utilizing the traditional electromagnetic scattering formalism. The resonances for the considered cavities have been identified via controlling their response along specific directions with help from phase diagram [22], by optimizing the textural contrast [23] or with maximizing the overall scattering efficacy [24]. Furthermore, the cloaking of quantum nanoinclusions has been the objective of several works by regulating the phase shift of each angular momentum channel [25], through tilting properly the nanorod axis [26, 27], via using the scattering cancellation principle applied in electrodynamics [28] or with exploiting Aharonov-Bohm effect [29]. Alternatively, vanishing perturbation of the background quantum signal has been achieved via the interplay among the nodal points of partial waves [30], through tailoring concentric layers for furtive detection [31], with employing anisotropic quantum materials [32] or by supporting internally trapped wave functions [33].

In this work, we examine the scattering of matter waves by nanospheres and nanowires embedded into certain backgrounds. Our target is to propose maximally or minimally engaging setups which, due to the resonant nature of the effects, will change substantially and in a stable manner their output for mild perturbations of their inputs. Such a behavior permits the reported optimized nanoinclusions to operate as efficient sensors for specific levels of energies, incidence angles and material characteristics; in particular, we are searching for superscattering nanospheres and tilted cloaked nanorods. The size of the considered cavities is chosen neither too small to avoid negligible scattering nor too big to admit the inclusions to work collectively in chain layouts of multiple elements; importantly, maxima and minima appearing at the boundaries of the parametric boxes are rejected. Accordingly, sharp variations of the scattering response from the corresponding optimal cavities, with respect to structural, textural and excitation characteristics of our setup, have been reported. The same approach described in this work can be adopted for alternative setups that exhibit interesting behavior when excited by electromagnetic waves like anisotropic inclusions [34], inhomogeneous scatterers [35], cavities hosted in different materials than the background [36] and inverse considerations [37]. Our results may inspire further theoretical and experimental efforts of building constitutive blocks or parts in integrating quantum sensing systems with extensive applications like single-photon detection and time-resolved photon counting.

2. MATHEMATICAL FORMULATION

2.1. Spherical Inclusion

In Fig. 1(a), we regard a plane matter wave representing a beam of particles with energy E that propagates into a medium with potential energy level V_0, where the electrons are traveling as if they have mass m_0 instead of m_e which is their inertial mass. It should be stressed that our consideration concerns either a single charged particle or an ensemble of particles that are moving coherently, namely, with identical stochastic characteristics and possessing the same energy. Importantly, we assume unimpeded flow of electron over relatively long distances in the background material (ballistic regime) while we ignore the presence of multiple valleys in the shape of wave bands. The incoming quantum signal meets a spherical inclusion of radius a that is filled by another medium with respective effective parameters (V, m). The wave function of the particle $\Psi(\mathbf{r})$ describing its stochastic motion along an axis z, is

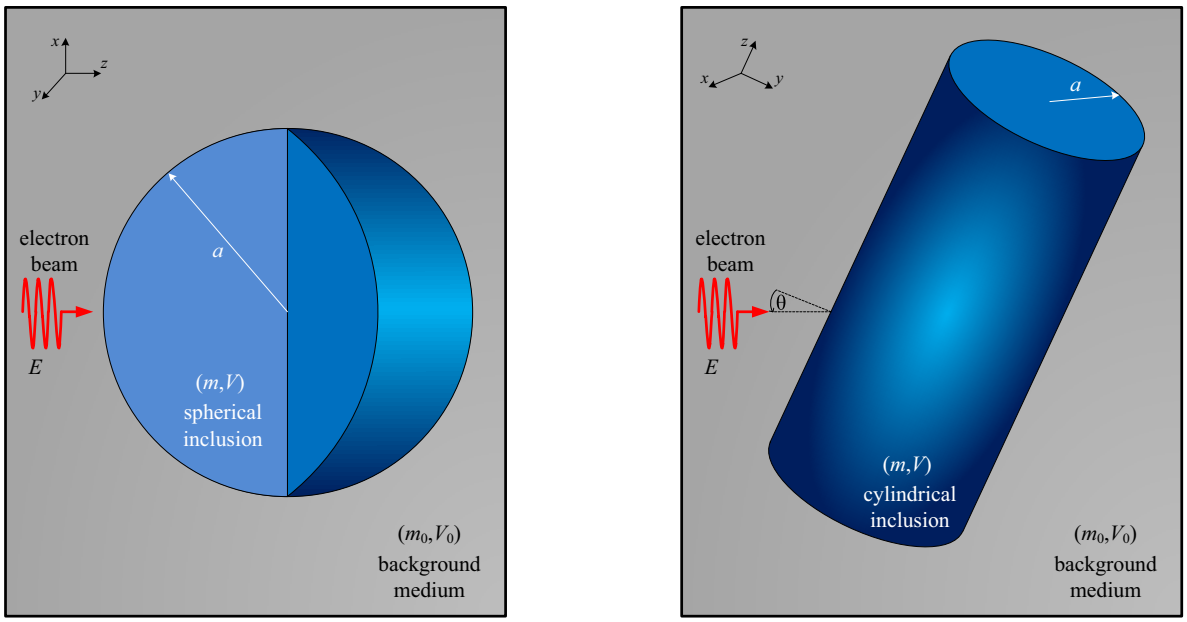

Figure 1. The physical configurations of the consider nanocavities. (a) Nanosphere of radius a, (b) nanocylinder of radius a, scattering an incoming matter plane wave of energy E. The nanocavities are filled with a medium with effective quantum characteristics (m, V) embedded in a background with effective quantum characteristics (m_0, V_0).

dependent on the associated spherical coordinates (r, θ, φ) and satisfies the time-independent, effective-mass Schrödinger equation [38]:

$$\nabla \left[\frac{1}{m(\mathbf{r})} \nabla \right] \Psi(\mathbf{r}) + \frac{E - V(\mathbf{r})}{\hbar^2/2} \Psi(\mathbf{r}) = 0, \tag{1}$$

where $\hbar$ is the reduced Planck constant. The potential energy in each region, expressing the energy required to extract a particle from the region into vacuum, is denoted by $V(\mathbf{r})$, while the effective mass, describing the band structure of the Floquet-Bloch waves created due to the crystalline texture, is denoted by $m(\mathbf{r})$. From the fundamentals of quantum mechanics [39], we know that, with the suitable normalization, the positive quantity $|\Psi(\mathbf{r})|^2$ is proportional to the probability of finding the electron at a point with position vector $\mathbf{r}$. In addition, the real vector:

$$\mathbf{J}(\mathbf{r}) = \frac{i\hbar}{2m(\mathbf{r})} \left[\Psi(\mathbf{r}) \nabla \Psi^*(\mathbf{r}) - \Psi^*(\mathbf{r}) \ \nabla \Psi(\mathbf{r}) \right] = -\frac{\hbar}{m(\mathbf{r})} \Im \left[\Psi(\mathbf{r}) \ \nabla \Psi^*(\mathbf{r}) \right] \tag{2}$$

is the so-called "probability current", the nearest thing one can have to describe the motion direction of a quantum particle [40]. Across the boundary of two regions with effective masses $\{m_1, m_2\}$ and wave functions $\{\Psi_1, \Psi_2\}$ respectively, the probability amplitudes and the probability currents flow should be continuous:

$$\Psi_1 = \Psi_2, \quad \frac{1}{m_1} \hat{\mathbf{n}} \cdot \nabla \Psi_1 = \frac{1}{m_2} \hat{\mathbf{n}} \cdot \nabla \Psi_2, \tag{3}$$

where $\hat{\mathbf{n}}$ is the unitary vector normal to the interface of the two media with direction from the first to the second one.

If the regarded electron in the absence of the spherical scatterer is forced to move along $+z$ axis with equal probability at every single point of the normal xy planes, its matter wave function is given by:

$$\Psi_{inc} = e^{ik_0 z} = \sum_{n=0}^{+\infty} i^n (2n+1) j_n(k_0 r) P_n(\cos\theta), \tag{4}$$

where $k_0=\sqrt{2m_0(E-V_0)}/\hbar=2\pi/\lambda$ is the wave vector norm into the background material, j_n the spherical Bessel function of order n, and P_n the Legendre polynomial of degree n. In the presence of the sphere, the aforementioned wave function, according to Mie theory [41], gets modified and takes the form:

$$\Psi(r,\theta)=\sum_{n=0}^{+\infty} i^n(2n+1)R(r)P_n(\cos\theta), \tag{5}$$

where:

$$R(r)=\begin{cases} C_n j_n(kr), & r<a \\ j_n(k_0 r)+S_n h_n(k_0 r), & r>a \end{cases}. \tag{6}$$

The first term of the formula for the wave function outside of the spherical inclusion concerns the incident component Ψ_{inc} of Eq. (4), while the second one corresponds to the scattering component Ψ_{scat}. It is clear that we use the partial wave formalism that has been established in electromagnetic scattering [42]. The notation h_n is used for the spherical Hankel function of first type and order n and $k=\sqrt{2m(E-V)}/\hbar$ equals the wave vector norm into the material of the spherical scatterer. The coefficients C_n, S_n for $n\in\mathbb{N}$ can be found by imposing the boundary conditions (3) at $r=a$ and they take the following explicit forms [43]:

$$\begin{aligned} C_n&=\frac{k_0 m\left[-i/(k_0a)^2\right]}{km_0 j_n'(ka)h_n(k_0a)-k_0 m j_n(ka)h_n'(k_0a)}, \\ S_n&=-\frac{km_0 j_n'(ka)j_n(k_0a)-k_0 m j_n(ka)j_n'(k_0a)}{km_0 j_n'(ka)h_n(k_0a)-k_0 m j_n(ka)h_n'(k_0a)}, \end{aligned} \tag{7}$$

where the prime denotes the derivative with respect to the entire argument. With no loss of generality [28, 24], we can assume that the potential energy of the background medium is zero ("ground state", $V_0\leftarrow 0$), by adjusting properly the potential levels inside the material of the scatterer: $V\leftarrow(V-V_0)$. In other words, the energy of the electron $E\leftarrow(E-V_0)$ expresses its difference from the original V_0. Opposite to electrodynamics, where the contrast between materials is expressed with ratios of permittivities, permeabilities and wave impedances, in quantum mechanics is the difference between the potential energies that affects the major characteristics of the matter waves.

By inspection of Eqs. (5) and (6), it is clear that the scattering component Ψ_{scat} of the wave function comprises multiple spherical wave terms $h_n(k_0r)$ for $n\in\mathbb{N}$ and thus affects the motion of the electron mainly along the radial $\hat{\mathbf{r}}$ direction. Inspired by analogous formulation in electrodynamic scattering [44] where Poynting theorem applies, we can compute the surface integral of the scattering probability current [45]:

$$P_{scat}=\int_{(s)}\mathbf{J}_{scat}(\mathbf{r})\cdot d\mathbf{s}=a^2\int_0^{2\pi}\int_0^{\pi}\hat{\mathbf{r}}\cdot\mathbf{J}_{scat}(r=a,\theta,\varphi)\sin\theta d\theta d\varphi \tag{8}$$

across the normal direction $d\mathbf{s}$ of any closed surface (s) containing the spherical scatterer. Such a positive (for $m_0>0$) quantity certainly expresses how significantly the impinging matter wave is affected in the presence of the scatterer. This P_{scat} should be compared with the corresponding quantity in the absence of the sphere while taking into account its size a. Indeed, since the particle is traveling into background along z axis, one should integrate the vector $\mathbf{J}_{inc}=(-\hbar/m_0)\Im[\Psi_{inc}\nabla\Psi_{inc}^*]$ (equaling to the probability current of the unperturbed motion of the particle) at the maximal xy cross section (s) of the sphere (which has been hypothetically removed) with $d\mathbf{s}=ds\hat{\mathbf{z}}$. In this way, one obtains the quantity $P_{inc}=\hbar k_0\pi a^2/m_0$ and, accordingly, the metric expressing how strong is our quantum scatterer for its size a, possesses the formula:

$$Q\equiv\frac{P_{scat}}{P_{inc}}=\frac{4}{(k_0a)^2}\sum_{n=0}^{+\infty}(2n+1)|S_n|^2. \tag{9}$$

The scattering efficiency of photonic scatterers is defined in an identical way [46]. The series in Eq. (9) converges rapidly since $|S_n|\sim\frac{|m-m_0|}{|m+m_0|}\sqrt{n}(e/2)^{2n}(k_0a/n)^{2n}$ for $n\to+\infty$. A substantial (positive) metric Q indicates the ability of an object with specific size to perturb the matter wave direction of propagation

and consequently to be perceived by e-beams traveling in its own spatial neighborhood. Reversely thinking, the same sphere with radius a can be used to effectively detect electrons of specific energy E in the context of Fig. 1(a). Consequently, maximal efficiencies Q can give quantum designs with several diverse utilities including high energy selectivity in particle flows, increased readability of inclusions in homogeneous backgrounds and successful quantum sensing with use of electron beams.

2.2. Cylindrical Inclusion

In Fig. 1(b), we consider a similar wave scattering problem to that in Fig. 1(a), where the quantum signal meets obliquely, under angle θ, a cylindrical inclusion of radius a. It should be noted that the length of the nanocavity is assumed infinite so that the formulated boundary value problem is analytically treatable. Such a convention can be feasible if the finite spatial front of the incident electron pulse illuminates the cylinder along a large distance (many wavelengths λ) of z axis. It is only then that the local dynamics and the interaction across the interfaces will be well-captured by the analytical solution [43, 47]. The incident wave function is expressed in the associated cylindrical coordinates (r, φ, z) as follows:

$$\Psi_{inc} = e^{ik_0(y\cos\theta + z\sin\theta)} = e^{ik_0 z\sin\theta}\sum_{n=-\infty}^{+\infty}(-1)^n J_n(k_0 r\cos\theta)e^{in\varphi}, \tag{10}$$

where J_n is the cylindrical Bessel function of n-th order. In analogy with Eq. (5), the presence of the nanorod modifies the wave function in its neighborhood, according to Mie theory treating electrodynamic scattering [41], and it takes the form:

$$\Psi(r,\varphi,z) = e^{ik_0 z\sin\theta}\sum_{n=-\infty}^{+\infty}(-1)^n R(r)e^{in\varphi}, \tag{11}$$

with, like in Eq. (6):

$$R(r) = \begin{cases} C_n J_n(\beta r), & r < a \\ J_n(k_0 r\cos\theta) + S_n H_n(k_0 r\cos\theta), & r > a \end{cases}, \tag{12}$$

where $\beta = \sqrt{k^2 - k_0^2\sin^2\theta}$ and H_n is the cylindrical Hankel function of first type and order n. Note that again partial wave formalism, routinely employed in electromagnetics, is adopted in Eq. (12) by writing each angular momentum channel $e^{in\varphi}$ as a separate term. Furthermore, by applying the necessary boundary conditions (3) for continuity of wave function and proportionality (with analogy constant m/m_0) of their normal derivatives at $r = a$ [38], one obtains the following explicit form of the complex coefficients C_n, S_n for $n \in \mathbb{Z}$:

$$\begin{aligned} C_n &= \frac{k_0 m[-2i/(\pi k_0 a)]}{\beta m_0 J_n'(\beta a)H_n(\beta_0 a) - \beta_0 m J_n(\beta a)H_n'(\beta_0 a)}, \\ S_n &= \frac{\beta_0 m J_n'(\beta_0 a)J_n(\beta a) - \beta m_0 J_n(\beta_0 a)J_n'(\beta a)}{\beta m_0 J_n'(\beta a)H_n(\beta_0 a) - \beta_0 m J_n(\beta a)H_n'(\beta_0 a)}, \end{aligned} \tag{13}$$

where $\beta_0 = k_0\cos\theta$.

A metric of how significantly the rod changes the background Ψ_{inc}, in its own vicinity, can be found by computing the probability current from Eq. (2) crossing the cylindrical boundary of the inclusion. As stated above, if we integrate the $\hat{\mathbf{r}}$ component of probability current around $r = a$, we derive the formula:

$$Q \equiv \frac{P_{scat}}{P'_{scat}} = \frac{\sum_{n=-\infty}^{+\infty}|S_n|^2}{\sum_{n=-\infty}^{+\infty}|S'_n|^2}. \tag{14}$$

The primed quantities P'_{scat} and $S'_n = -J_n(\beta_0 a)/H_n(\beta_0 a)$ concern a strong scatterer of the same size $2a$, that demands a vanishing wave function ($\Psi = 0$) across its volume, namely the quantum analogue

of the perfect electric conductor (PEC) of classical electrodynamics. The convergence of both the series in Eq. (14), exactly as happening with Eq. (9), is quite fast as long as the quantity $k_0 a$ is not huge: $|S_n| \sim \frac{|m-m_0|}{|m+m_0|}\sqrt{|n|}(e/2)^{2|n|}(k_0 a/|n|)^{2|n|}$ and $|S_n'| \sim \sqrt{|n|}(e/2)^{2|n|}(k_0 a/|n|)^{2|n|}$ for $|n| \to +\infty$.

It should be remarked that a sensing purpose is served not only by a large Q but also by a vanishing one; indeed, what counts is how sharp the response changes when the controlling parameter is perturbed and not the actual value of response. Therefore, in order to avoid overlapping information with the results for nanospheres of maximum scattering efficiency in Eq. (9), our aim in that nanowire scenario is to minimize the modified scattering metric of Eq. (14). When Q is very small, we have the case of an elongated inhomogeneity that suppresses substantially its own response, renders itself effectively invisible (cloaked) to impinging electrons and totally free to record their movement. Importantly, such a perfect cloaking regime prevents also the cavity from being found by the probing particle beams but it would be completely detectable once the cloaking conditions cease to exist; that is a characteristic of a sensor.

3. QUANTUM SENSING WITH NANOSPHERES

In order to select the best spherical setups of Fig. 1(a) for sensing quantum waves, we assume that the effective masses in both regions (background and inclusion) are equal to the inertial mass of electron: $m_0 = m = m_e$, regardless of the direction that the particle is traveling. In addition, we consider potential energy levels for both the areas that cover a substantial range, namely $0\,\text{eV} < V < 10\,\text{eV}$ and $1\,\text{eV} < V_0 < 11\,\text{eV}$, while the regarded quantum beams can possess energy E belonging to the interval $0\,\text{eV} < E < 1\,\text{eV}$. When it comes to the radius a of the spherical cavity, it is selected between a lower limit to avoid artifacts of maximum Q by a poor scatterer due to the presence of P_{inc} (being proportional to size $k_0 a$) in the denominator of (9) and an upper limit that permits the nanosphere to work collectively with other similar scatterers in a chain quantum setup [48]; thus, $0.05 < a/\lambda < 0.2$ where $\lambda = 2\pi/k_0$. In Fig. 2, we present the results for our optimization on (V_0, E) map; at each point of this plane, we find the maximum Q by sweeping the size a/λ and the potential of the cavity medium V before we record the optimal setup. Our mission is to put the maximum "in a box", namely trapping the peak of the recorded quantity Q into the $(a/\lambda, V)$ rectangular domain defined by the aforementioned inequalities; accordingly, we reject the configurations exhibiting boundary extrema where the maximum Q is found at the boundaries of the optimization parametric box [49]. In such cases, we leave the

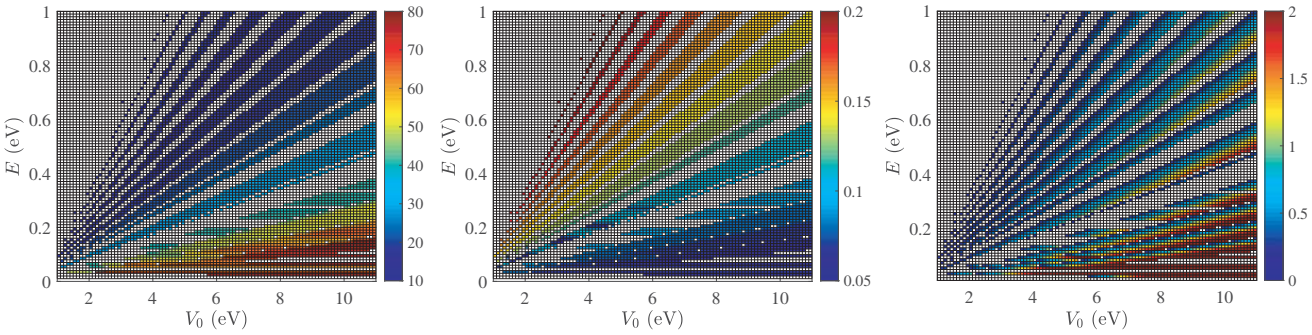

Figure 2. The results of our optimization for nanosphere scattering sensors by sweeping the inclusion radius a/λ and the potential level of the material filling the cavity V. (a) The maximal scattering efficiency Q of Eq. (9), (b) the radius a of the optimal design normalized by the oscillation wavelength λ of the incoming natter wave, (c) the optimal potential energy levels V of the cavity materials in eV, for various background potential energy levels V_0 and several impinging energies E of the e-beams. Assumptions: $m_0 = m = m_e$, where m_e is the inertial mass of electron, along all the three directions of the three-dimensional space. White pixels correspond to combinations that the maximum scattering cannot be trapped internally to the regarded $(a/\lambda, V)$ optimization box.

corresponding pixel on the (V_0, E) map empty (white) since the actual resonance occurs outside of the regarded $(a/\lambda, V)$ region within which we have agreed to perform the parametric sweeps.

In Fig. 2(a), we show the maximum Q obtained via the process described above; one can clearly notice that the performance is higher for small impinging energies E and higher host potential levels V_0. However, in most of the considered combinations, we obtain high Q, a feature that renders the corresponding optimal setups suitable to work as quantum sensors. Note that for higher energies E and lower potentials V, one can hardly find any acceptable optimal solution; however, while blank radial strips (with $E/V \cong$ constant) are also appearing across the entire map alternated with valid extrema. In Fig. 2(b), we show the optimal dimension of the radius a normalized by the operational wavelength $\lambda = 2\pi\hbar/\sqrt{2m_0 E}$ (different for each incident energy E), that give the maximal performances in Fig. 2(a). It is observed that smaller nanospheres give higher scattering efficiencies, a fact that can be attributed to the definition of Q in (9). In Fig. 2(c) we represent the corresponding optimal potentials V of the spherical cavities that are kept moderate with the exception of lower right corner which leads to more significant scores, as indicated by Fig. 2(a).

In Fig. 3, we observe the influence of a different effective mass into the cavity on some characteristic optimal designs of Fig. 2(a). In particular, we keep the same all the other parameters and represent the scattering metric Q as a function of the impinging energy E for various $m \cong m_e$. In Fig. 3(a), we regard a sensor working at $E = 0.15\,\text{eV}$ and notice that once the effective mass becomes smaller, the response gets weaker and the maximum is appeared at larger energies E. A similar trend is recorded in Fig. 3(b), where a design operated at higher energy levels $E = 0.5$ eV is examined; in such a case, the represented scores are lower, as also revealed by Fig. 2(a), and the influence of effective mass miscalculation m less severe than Fig. 3(a).

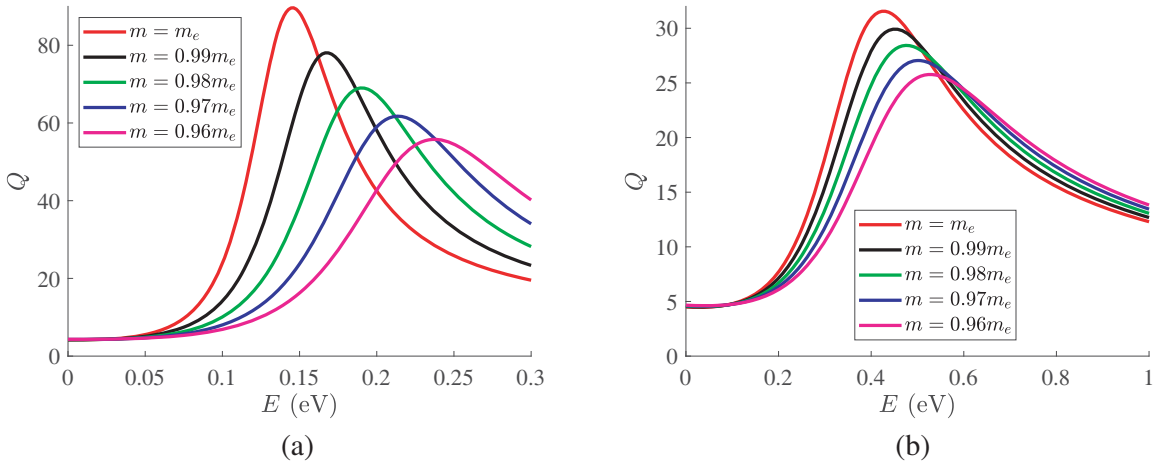

Figure 3. The scattering efficiency Q of nanospheres given by Eq. (9), as function of the incoming energy E for various effective masses m of the material filling the nanocavity. The optimization has been executed for $m = m_e$. (a) $E = 0.15\,\text{eV}$, $a/\lambda = 0.06$, (b) $E = 0.5\,\text{eV}$, $a/\lambda = 0.11$.

In Fig. 4(a), we represent the scattering efficiency Q as a function of radius a/λ for three distinct setups of various optimal dimensions operated at different background potentials V_0; the optimal regimes are marked by circular dots. One can clearly observe the very sharply changing responses with huge maxima Q; such a characteristic makes the reported optimal designs extremely suitable as sensors of specific inclusion sizes. In addition, we note that thicker structures can give even more highly selective resonances while due to the adopted resolution in our optimization, the absolute maximum can slightly differ (and be more substantial) from the one indicated by the marker. In Fig. 4(b), we repeat the same process but for nanospheres operated at higher energies E that give lower performances as also conveyed by Figs. 2(a) and 3. The lineshapes are changing less abruptly and again, as happening in Fig. 3(b), a smaller host potential V_0 gives lower scattering efficiencies Q and thicker optimal nanocavities.

In Fig. 5, we investigate how the scattering performance in dB $10\log Q$ is modified when a mistaken engineering has led to wrong estimation of the potential levels (V_0, V) while the actual ones are denoted

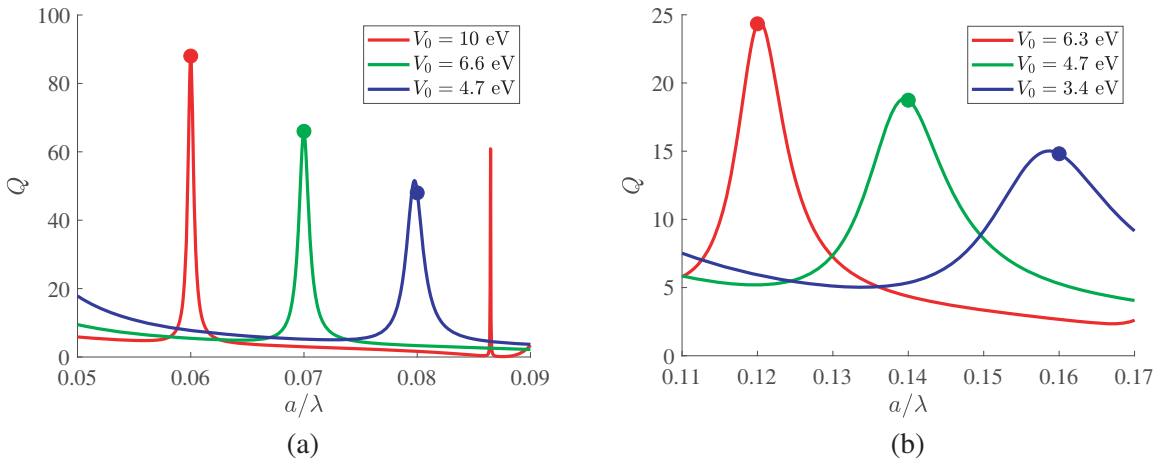

Figure 4. The scattering efficiency Q given by Eq. (9), as function of nanosphere radius a divided by the oscillation wavelength λ for various designs working with different background potential levels V_0; the optimal sizes are denoted by circular markers. (a) $E = 0.12\,\text{eV}$, (b) $E = 0.4\,\text{eV}$.

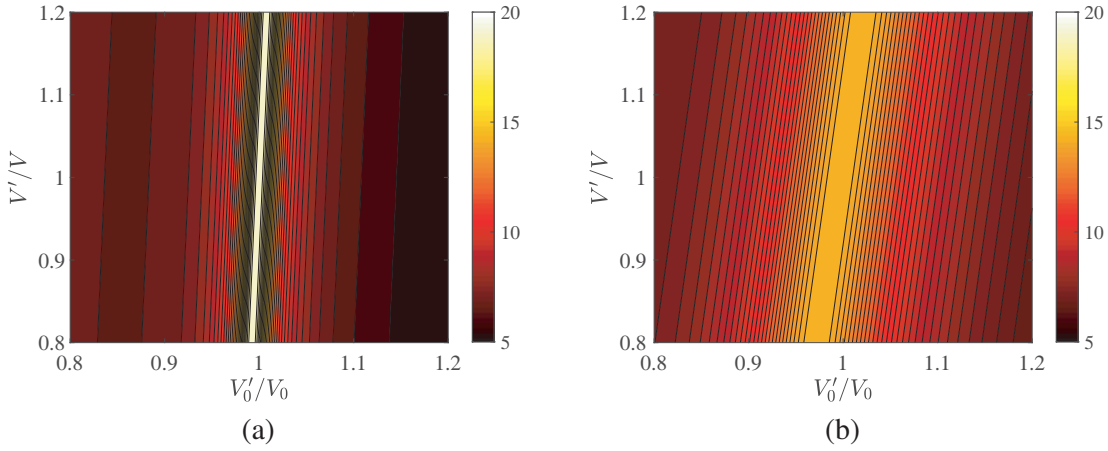

Figure 5. The scattering efficiency Q given by Eq. (9), in dB, of optimal nanospheres when the potential energy levels for the background and the inclusion (V_0, V) are mis-estimated compared to their true values (V_0', V') with respect to whom the optimization was carried out. (a) $V_0 = 10.4\,\text{eV}$, $V = 0.4\,\text{eV}$, $a/\lambda = 0.06$, $E = 0.15\,\text{eV}$. (b) $V_0 = 10.5\,\text{eV}$, $V = 1.3\,\text{eV}$, $a/\lambda = 0.11$, $E = 0.5\,\text{eV}$.

by primed symbols (V_0', V'). It is remarkable that an almost vertical, thin strip of high-Q is formed, unveiling the higher sensitivity of the design to changes of V_0 and its relative robustness with respect to V. Such a behavior is owed to the much larger magnitude of V_0 than V that is also reflected in Fig. 2(c). By inspection of Fig. 5(a), we realize how selective the reported resonances are and how the respective layouts can serve the purpose of sensing; indeed, such a setup can sharply detect specific potential levels V_0 of background. In Fig. 5(b), we consider a less successful design and, for the same relative deviations from the optimal values, a higher robustness in the response indicating stability of the resonances with respect to small perturbations, is remarked.

To demonstrate the strong scattering effect reported by Figs. 2(a), 4, 5, we evaluate the probability $|\Psi(x, y = 0, z)|^2$ on the (z, x) plane divided by its maximal value $\Psi_{\text{max}} = \max_{(x,z)} |\Psi(x, y = 0, z)|$. In Fig. 6(a), we regard a setup operated under small-energy illumination along z axis and a high signal concentration is observed into and in the vicinity of the nanosphere while a dipolar scattering pattern is formed. In Fig. 6(b), where an optimized design working at a mid-energy level and a larger scatterer is considered, we notice a much larger probability across the external region combined with the appearance

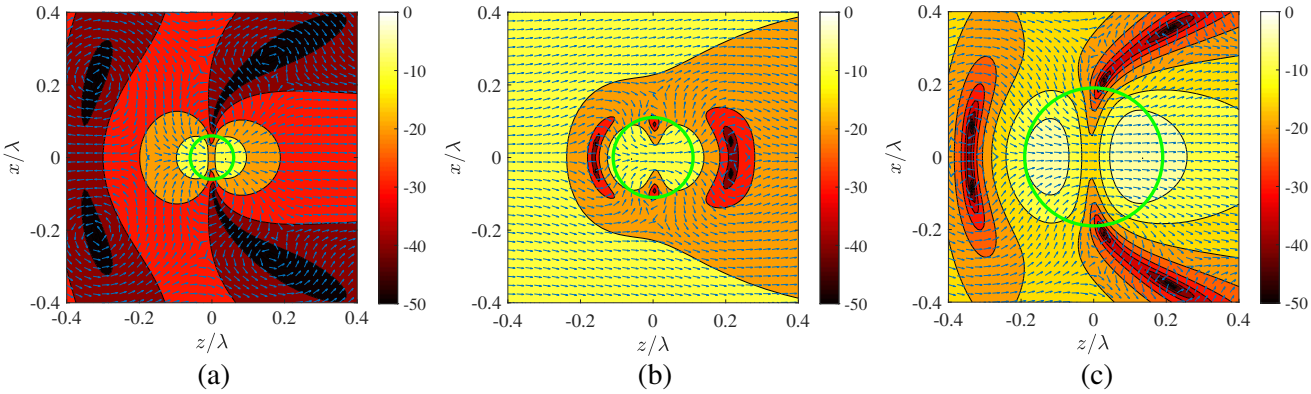

Figure 6. Spatial distribution of (normalized) probability $|\Psi(x,y,z)|^2/\Psi^2_{\max}$ in dB across y plane for: (a) low-energy optimal design ($E = 0.15\,\text{eV}$, $V_0 = 10.4\,\text{eV}$, $V = 0.4\,\text{eV}$), (b) mid-energy optimal design ($E = 0.4\,\text{eV}$, $V_0 = 10.5\,\text{eV}$, $V = 1.3\,\text{eV}$), (c) high-energy optimal design ($E = 0.62\,\text{eV}$, $V_0 = 3.6\,\text{eV}$, $V = 0.3\,\text{eV}$). The blue arrows show the transverse direction of probability current $\mathbf{J}$ at a fixed y plane and the green solid line the circular boundary of the sphere.

of a shading behind the cavity. Finally, in Fig. 6(c), we investigate the case of an even more bulky sphere than the operational wavelength λ which is shorter due to the increased level of energy E. One directly observes the standing pattern that is created for $z < 0$ while zones of vanishing Ψ are developed for $z > 0$, even though the probability of tunneling through the scatterer is quite high.

4. QUANTUM SENSING WITH NANOCYLINDERS

The main difference between the nanocylinder scattering of Fig. 1(b) and the corresponding one of the spherical nanocavity in Fig. 1(a) is that the response of the former one depends on the angle θ. Thus, we modify the optimization scheme described for the first problem and additionally sweep that extra variable: $0^\circ < \theta < 90^\circ$. However, we will keep the parameters of the material filling the cavity, fixed: $V = 1.5\,\text{eV}$, $m = 0.1m_e$ (resembling semi-conductors like GaAs [50]) and the search for extrema will occur across $(a/\lambda, \theta)$ box. The range for the radius a is identical to that of the previous optimization $0.05 < a/\lambda < 0.2$ for the same reasons mentioned above. As far as the background potential level V_0 is concerned, it can vary within the interval: $6\,\text{eV} < V_0 < 16\,\text{eV}$ while $m_0 = m_e$; indeed, we are searching for cloaked cylinders and thus a substantial textural contrast between the two media is a prerequisite, otherwise the problem is trivial. It is noted that the minimization of Q occurs for low energies [26] and thus we consider electron beams with $0.01\,\text{eV} < E < 0.09\,\text{eV}$.

In Fig. 7(a), we show the inverse metric $1/Q$ in dB, and we realize that the suppression of scattering by four orders of magnitude is possible at every single energy level E as long as V_0 is chosen properly. There are several infeasible combinations of (V_0, E) sporadically across the entire map of Fig. 7(a); however, it seems that for low V_0 (as happening also in Fig. 2(a)) is harder to find a non-boundary extremum within the regarded $(a/\lambda, \theta)$ optimization box. In Fig. 7(b), we show the optimal values of the normalized radius a/λ for which the peak performances reported in Fig. 7(a) are exhibited; there is a clear trend that thicker designs are obtained as the energy E increases combined with a decline in V_0. In Fig. 7(c), we show the angles θ in degrees for which substantial suppression of scattering by the wire is recorded. It is noteworthy that most optimal cloaking regimes occur for very oblique directions of incidence.

In Fig. 8(a), we show the scattering efficiency in Eq. (14) as a function of the incident beam's energy E for various optimal designs operated at different levels of energies and at different beam directions θ. The setups hosting these sharp resonances can work as very efficient selectors of E and thus quantum sensing becomes feasible. In Fig. 8(b), we represent the metric Q of the same layouts but when illuminated at a common angle $\theta = 60^\circ$ instead of the optimal ones (in Fig. 8(a)). The resonances are becoming less abrupt and occurring at slightly larger frequencies but still a filtering operation can

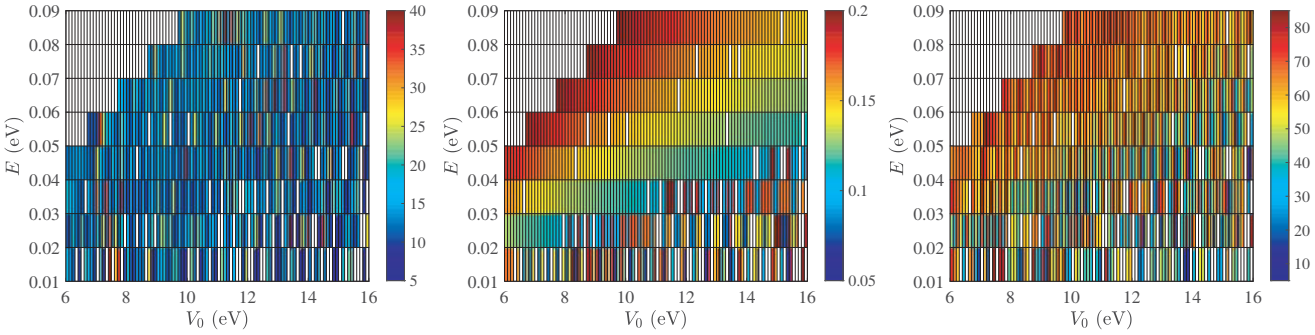

Figure 7. The results of our optimization for the tilted nanowires. (a) The inverse scattering efficiency $1/Q$ from Eq. (14) in dB, (b) the radius a of the optimal nanocavity divided by the operational wavelength λ, (c) the optimal incident angle θ (in degrees), for various background potential levels V_0 and incoming particle energies E. Assumptions: $m_0 = m_e$, $m = 0.1m_e$, $V = 1.5\,\text{eV}$ where m_e is the inertial mass of electron. White pixels correspond to combinations that the maximum scattering cannot be trapped internally to the regarded $(a/\lambda, \theta)$ optimization box.

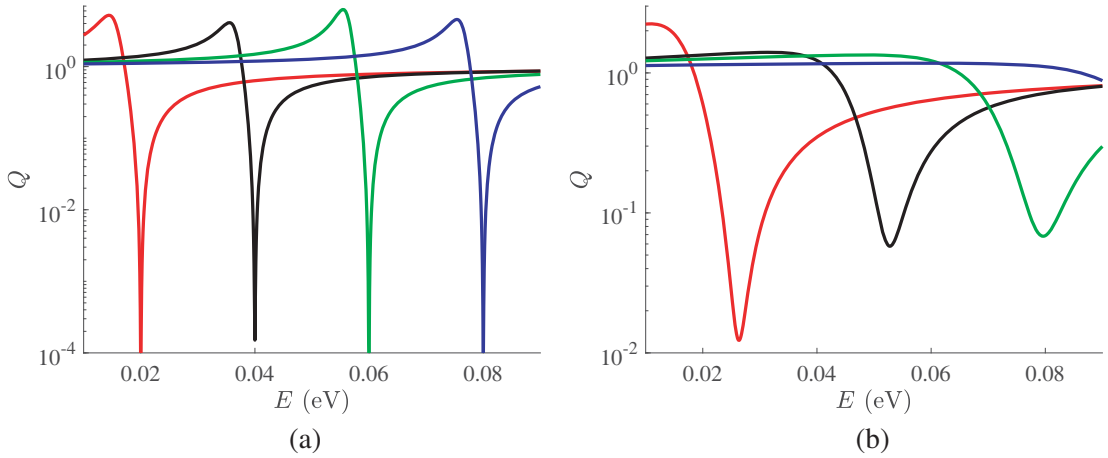

Figure 8. The scattering efficiency Q of cylindrical nanocavities from Eq. (14) as a function of impinging energy E of the particles. (a) Optimized designs, operated obviously at different energies E under different optimal angles θ. (b) The same designs under an arbitrary oblique incidence ($\theta = 60°$).

be supported.

In Fig. 9, we perform similar computations to those of Fig. 4 but for cloaked nanorods this time. In Fig. 9(a), the metric Q from Eq. (14) is represented as a function of a/λ, where the optimal operational points are indicated by circular markers. We notice that the scattering gets substantially mitigated and that cloaking regime is very sensitive to changes in radius a. Furthermore, additional resonances either of minimum or maximum Q emerge along a/λ axis which, due to their large figure of merit, can be also exploited for sensing scopes. In Fig. 9(b), we repeat the calculations but the incidence angle is now sub-optimally selected and kept fixed at $\theta \cong 60°$, as in Fig. 8(b). We understand that each of the designs, operated at different energy levels E, gives milder variations with respect to a/λ, similarly to Fig. 8(b).

In Fig. 10, we investigate the response of structures optimized for specific size a operated under certain energy levels E when the corresponding actual parameters are different (a', E'), similarly to what we did in Fig. 5 for the nanosphere designs. It is remarkable that the response from the optimized cavities is much more sensitive to a deviation of size a than to the same relative perturbation of energy

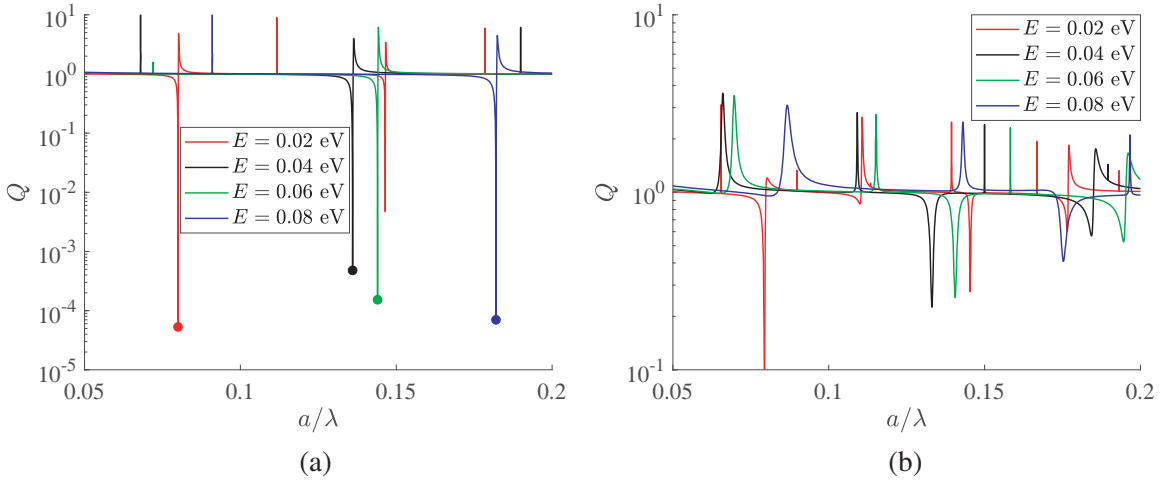

Figure 9. The scattering efficiency Q of nanorods of Eq. (14) as a function of the radius a/λ. (a) Optimized designs, operated at different energies E, under different optimal angles θ and with their operational points denoted by circular markers. (b) The same designs under an arbitrary oblique incidence ($\theta = 60°$).

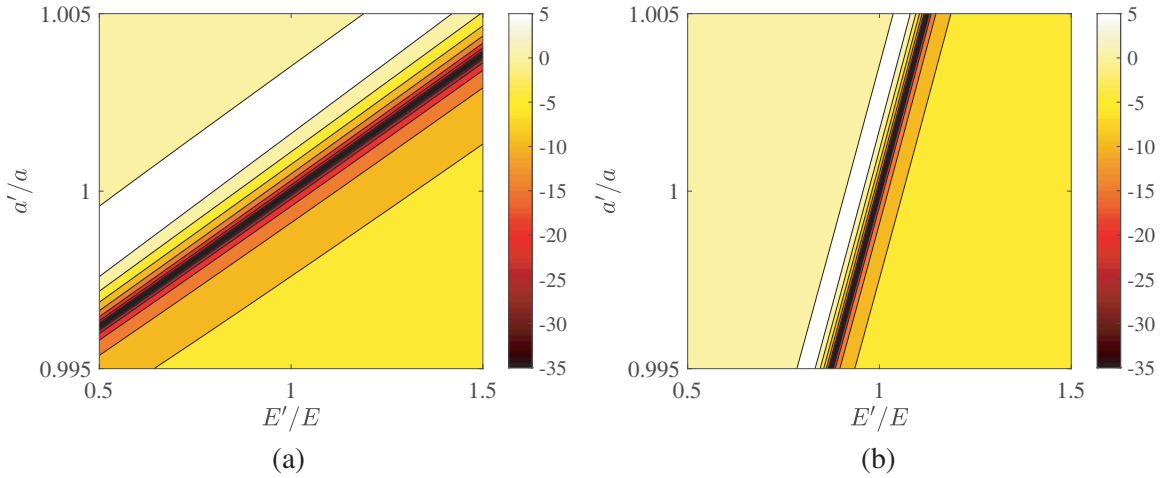

Figure 10. Robustness of the scattering efficiency Q from Eq. (14) for small changes of the cavity potential level V' and the geometrical radius a' of the cylinder around the optimal values (V, a). (a) $E = 0.01\,\text{eV}$, $V_0 = 13.3\,\text{eV}$, $a/\lambda = 0.08$. (b) $E = 0.08\,\text{eV}$, $V_0 = 9.9\,\text{eV}$, $a/\lambda = 0.136$.

E. Such a characteristic is also demonstrated by Fig. 9 where the slightest change of a destroys the cloaking equilibrium; on the contrary, Fig. 7 shows the emergence of that interesting effect at almost the same impinging energy level E despite a substantial change in the incidence angle θ. What is also notable, is that dark strips indicating a perfect cloaking are accompanied by additional parallel strips of maximal scattering revealing the pattern of Fano resonances [51], particularly befitting to sensing applications. By comparing Fig. 10(a) with Fig. 10(b), we notice that the second design is less robust with respect to the same relative modification of E, since its operational energy ($E = 0.08\,\text{eV}$) is eight times higher than the first one ($E = 0.01\,\text{eV}$) and thus it corresponds to larger absolute shifts.

Having understood the influence of the background medium (effective mass m_0, potential V_0) and the characteristics of the incoming beam (energy E, angle θ) on the sharp response of optimal setups working at a cloaking resonance, it is meaningful to observe the spatial variation of the actual quantum signal (wave function Ψ). In Fig. 11, we show the probability of finding the particle at a

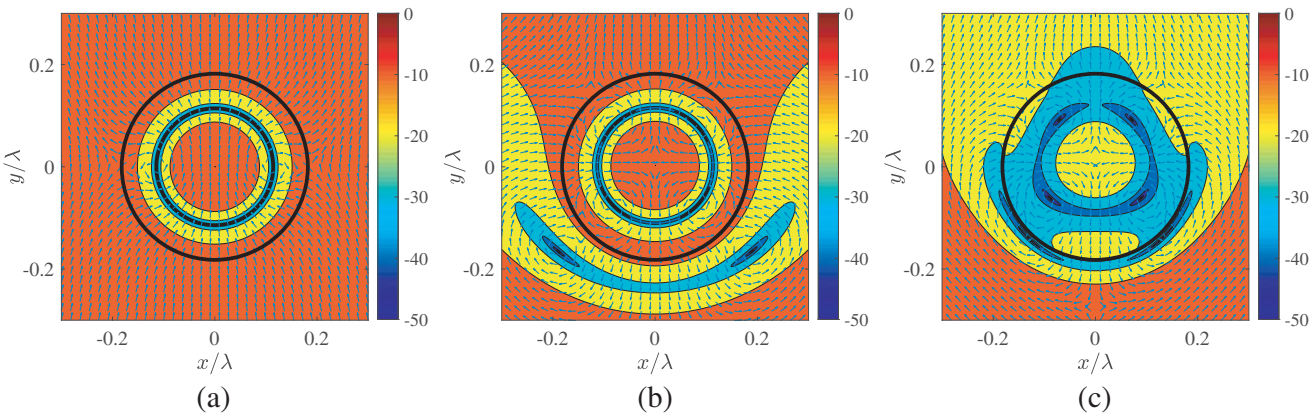

Figure 11. Spatial distribution of (normalized) probability $|\Psi(x,y,z)|^2/\Psi_{\max}^2$ in dB for: (a) optimal incidence angle that can achieve cloaking ($\theta \cong 87^\circ$), (b) $\theta = 60^\circ$, (c) normal incidence ($\theta = 0^\circ$). The blue arrows show the transverse direction of probability current $\mathbf{J}$ at a fixed z plane and the black solid line the circular boundary of the rod. Plot parameters: $E = 0.08\,\text{eV}$, $V_0 = 11.2\,\text{eV}$. The plane matter wave is propagated along the positive y axis and the obtained result is not dependent from the selection of z variable.

specific point across the plane (x,y) and the arrows on top of the contour correspond to the probability current $\mathbf{J}$ from Eq. (2). The represented quantity is normalized in dB: $20\log(|\Psi(x,y,z)|/\Psi_{\max})$, where $\Psi_{\max} = \max_{(x,y)}|\Psi(x,y,z)|$; note that $|e^{ik_0 z\sin\theta}| = 1$ and thus the selection of z does not affect the result $|\Psi|^2$ from Eq. (10). In Fig. 11(a), we regard a cloaking case and one can observe that the probability current propagated along y axis according to Eq. (10), is almost unperturbed externally to the scatterer; it is also noticed the ring of vanishing probability created internally to the rod. In Fig. 11(b), we repeat the calculations for a non-optimal direction $\theta = 60^\circ$; therefore, moderate back-scattering is recorded while two "whirlpools" of probability current around points of vanishing probability are developed for $y < 0$. In Fig. 11(c), we examine the normal incidence scenario ($\theta = 0^\circ$) for the same cylinder, where the reflections are even more significant than in Fig. 11(b) and the pattern into the cross section of the rod becomes more complicated and less azimuthally symmetric.

5. CONCLUSIONS

Quantum metrology and quantum sensing study parameter estimation limits in various physical systems by employing the fundamental laws of quantum physics and have recently attracted significant scientific and funding attention. The backbone behind the corresponding designs is the sharp variation of the quantum response with respect to one or more controlling parameters and this purpose is found to be well-served by the scattering of matter waves from nanoinclusions. The size of nanospheres and nanowires are carefully paired with the filling media and the impinging excitation in order to scatter maximally or minimally the incoming electron beam and exhibit high energy and angle selectivity, a prerequisite for efficient sensing.

An interesting expansion of the present work would be to consider multiple nanoinclusions like the aforementioned ones to operate collectively in a quantum metasurface layout. The extreme scattering effects from each of the cavities will create matter wave fronts that can be used to spatially tailor the reflection and transmission probabilities based on the single-particle interaction with the structure. Components like these would be exceptionally befitted in a variety of integrated quantum systems from anomalous reflectors working as multiport quantum networks with controllable probabilities per channel to quantum memory elements where the signal gets trapped into close loops [52]. Finally, the presented approach can be used for the study of fundamental electrical properties of engineered nanoscaled devices operating in the quantum regime. It may eventually lead to the design of new kinds of nanomaterials, where functionality and structure of quantum nanodevices are described through electrical transport measurements and quantum phenomena such as superposition or entanglement.

ACKNOWLEDGMENT

This work was partially supported by Nazarbayev University Faculty Development Competitive Research Grant No. 021220FD4051 (*"Optimal design of photonic and quantum metamaterials"*).

REFERENCES

1. Giovannetti, V., S. Lloyd, and L. Maccone, "Quantum-enhanced measurements: Beating the standard quantum limit," *Science*, Vol. 306, 1330, 2004.
2. Degen, C. L., F. Reinhard, and P. Cappellaro, "Quantum sensing," *Rev. Mod. Phys.*, Vol. 89, 035002, 2017.
3. Schirhag, R., K. Chang, M. Loretz, and C. L. Degen, "Nitrogen-vacancy centers in diamond: Nanoscale sensors for physics and biology," *Annu. Rev. Phys. Chem.*, Vol. 65, 83, 2014.
4. Zaiser, S., T. Rendler, I. Jakobi, T. Wolf, S.-Y. Lee, S. Wagner, V. Bergholm, T. Schulte-Herbruggen, P. Neumann, and J. Wrachtrup, "Enhancing quantum sensing sensitivity by a quantum memory," *Nat. Commun.*, Vol. 7, 12279, 2016.
5. Pirandola, S., B. R. Bardhan, T. Gehring, C. Weedbrook and S. Lloyd, "Advances in photonic quantum sensing," *Nat. Photonics*, Vol. 12, 724, 2018.
6. Ajoy, A., Y.-X. Liu, K. Saha, L. Marseglia, J.-C. Jaskula, U. Bissbort, and P. Cappellaro, "Quantum interpolation for high-resolution sensing," *Proc. Natl. Acad. Sci. U.S.A.*, Vol. 114, 2149, 2017.
7. Bonato, C., M. S. Blok, H. T. Dinani, D. W. Berry, M. L. Markham, D. J. Twitchen, and R. Hanson, "Optimized quantum sensing with a single electron spin using real-time adaptive measurements," *Nat. Nanotechnol.*, Vol. 11, 247, 2016.
8. Istrate, E. and E. H. Sargent, "Photonic crystal heterostructures and interfaces," *Rev. Mod. Phys.*, Vol. 78, 455, 2006.
9. Fleury, R. and A. Alù, "Exotic properties and potential applications of quantum metamaterials," *Appl. Phys. A*, Vol. 109, 781, 2012.
10. Fleury, R. and A. Alù, "Manipulation of electron flow using near-zero index semiconductor metamaterials," *Phys. Rev. B*, Vol. 90, 035138, 2014.
11. Valagiannopoulos, C., "Optimized quantum filtering of matter waves with respect to incidence direction and impinging energy," *Quantum Eng.*, Vol. 2, e52, 2020.
12. Valagiannopoulos, C., "Quantum Fabry-Perot resonator: Extreme angular selectivity in matter-wave tunneling," *Phys. Rev. Appl.*, Vol. 12, 054042, 2019.
13. Valagiannopoulos, C., "Optimally sharp energy filtering of quantum particles via homogeneous planar inclusions," *Sci. Rep.*, Vol. 10, 816, 2020.
14. Ogawana, T. and H. Sakaguchi, "Transmission coefficient from generalized Cantor-like potentials and its multifractality," *Phys. Rev. E*, Vol. 97, 012205, 2018.
15. Valagiannopoulos, C., "Predicting the quantum texture from transmission probabilities," *J. Appl. Phys.*, Vol. 127, 174301, 2020.
16. Christesen, J. D., C. W. Pinion, D. J. Hill, S. Kim, and J. F. Cahoon, "Chemically engraving semiconductor nanowires: Using three-dimensional nanoscale morphology to encode functionality from the bottom up," *J. Phys. Chem. Lett.*, Vol. 7, 685, 2016.
17. Gazibegovic, S., et al., "Epitaxy of advanced nanowire quantum devices," *Nature*, Vol. 548, 434, 2017.
18. Hausmann, B. J. M., M. Khan, Y. Zhang, T. M. Babinec, K. Martinick, M. McCutcheon, P. R. Hemmerd, and M. Lončar, "Fabrication of diamond nanowires for quantum information processing applications," *Diam. Relat. Mater.*, Vol. 19, 621, 2010.
19. Tom, R. T., A. S. Nair, N. Singh, M. Aslam, C. L. Nagendra, R. Philip, K. Vijayamohanan, and T. Pradeep, "Freely dispersible Au@TiO_2, Au@ZrO_2, Ag@TiO_2, and Ag@ZrO_2 core-shell nanoparticles: One-step synthesis, characterization, spectroscopy, and optical limiting properties," *Langmuir*, Vol. 19, 3439, 2003.

20. Xu, L., M. Sun, W. Ma, H. Kuang, and C. Xu, "Self-assembled nanoparticle dimers with contemporarily relevant properties and emerging applications," *Materials Today*, Vol. 19, 595, 2016.
21. Ko, H.-W., M.-H. Chi, C.-W. Chang, C.-W. Chu, K.-H. Luo, and J.-T. Chen, "Fabrication of core-shell polymer nanospheres in the nanopores of anodic Aluminum oxide templates using polymer blend solutions," *ACS Macro Letters*, Vol. 4, 717, 2015.
22. Lee, J. Y. and R.-K. Lee, "Exploring matter wave scattering by means of the phase diagram," *EPL*, Vol. 124, 30006, 2018.
23. Valagiannopoulos, C., "Maximal quantum scattering by homogeneous spherical inclusions," *Phys. Rev. B*, Vol. 100, 035308, 2019.
24. Lee, J. Y., A. E. Miroshnichenko, and R.-K. Lee, "Designing quantum resonant scatterers at subwavelength scale," *Phys. Lett. A*, Vol. 381, 2860, 2017.
25. Liao, B., M. Zebarjadi, K. Esfarjani, and G. Chen, "Cloaking core-shell nanoparticles from conducting electrons in solids," *Phys. Rev. Lett.*, Vol. 109, 126806, 2012.
26. Valagiannopoulos, C., "Perfect quantum cloaking of tilted cylindrical nanocavities," *Phys. Rev. B*, Vol. 101, 195301, 2020.
27. Valagiannopoulos, C., E. A. Marengo, A. G. Dimakis, and A. Alù, "Aharonov-Bohm-inspired tomographic imaging via compressive sensing," *IET Microw. Antennas Propag.*, Vol. 12, 1890, 2018.
28. Fleury, R. and A. Alù, "Quantum cloaking based on scattering cancellation," *Phys. Rev. B*, Vol. 87, 045423, 2013.
29. Valagiannopoulos, C., A. N. Askarpour, and A. Alù, "Aharonov-Bohm detection of two-dimensional magnetostatic cloaks," *Phys. Rev. B*, Vol. 92, 224414, 2015.
30. Lee, J. Y. and R.-K. Lee, "Hiding the interior region of core-shell nanoparticles with quantum invisible cloaks," *Phys. Rev. B*, Vol. 89, 155425, 2014.
31. Fleury, R. and A. Alù, "Furtive quantum sensing using matter-wave cloaks," *Phys. Rev. B*, Vol. 87, 201106(R), 2013.
32. Zhang, S., D. A. Genov, C. Sun, and X. Zhang, "Cloaking of matter waves," *Phys. Rev. Lett.*, Vol. 100, 123002, 2008.
33. Greenleaf, A., Y. Kurylev, M. Lassas, and G. Uhlmann, "Approximate quantum cloaking and almost-trapped states," *Phys. Rev. Lett.*, Vol. 101, 220404, 2008.
34. Valagiannopoulos, C. A., "Study of an electrically anisotropic cylinder excited magnetically by a straight strip line," *Progress In Electromagnetics Research*, Vol. 73, 297, 2007.
35. Valagiannopoulos, C. A., "Arbitrary currents on circular cylinder with inhomogeneous cladding and RCS optimization," *Journal of Electromagnetic Waves and Applications*, Vol. 21, No. 5, 665–680, 2007.
36. Valagiannopoulos, C. A., "Closed-form solution to the scattering of a skew strip field by metallic pin in a slab," *Progress In Electromagnetics Research*, Vol. 79, 1, 2008.
37. Valagiannopoulos, C. A., "A novel methodology for estimating the permittivity of a specimen rod at low radio frequencies," *Journal of Electromagnetic Waves and Applications*, Vol. 24, No. 5–6, 631–640, 2010.
38. Trachanas, S., *An Introduction to Quantum Physics: A First Course for Physicists, Chemists, Materials Scientists, and Engineers*, John Wiley & Sons, New York, USA, 2018.
39. Griffiths, D. J., *Introduction to Quantum Mechanics*, Pearson Prentice Hall, New Jersey, USA, 2005.
40. Hodge, W. B., S. V. Migirditch, and W. C. Kerr, "Electron spin and probability current density in quantum mechanics," *Am. J. Phys.*, Vol. 82, 681, 2014.
41. Balanis, C. A., *Advanced Engineering Electromagnetics*, John Wiley & Sons, New York, USA, 2012.
42. Osipov, A. V. and S. A. Tretyakov, *Modern Electromagnetic Scattering Theory with Applications*, John Wiley & Sons, New York, USA, 2017.

43. Valagiannopoulos, C. A., "Single-Series Solution to the Radiation of Loop Antenna in the Presence of a Conducting Sphere," *Progress In Electromagnetics Research*, Vol. 71, 277, 2007.
44. Sheverdin, A. and C. Valagiannopoulos, "Core-shell nanospheres under visible light: Optimal absorption, scattering, and cloaking," *Phys. Rev. B*, Vol. 99, 075305, 2019.
45. Cohen-Tannoudji, C., B. Diu, and F. Laloe, *Quantum Mechanics*, John Wiley & Sons, New York, USA, 1992.
46. Bohren, C. F. and D. R. Huffman, *Absorption and Scattering of Light by Small Particles*, John Wiley & Sons, New York, USA, 1983.
47. Valagiannopoulos, C. A., "An overview of the Watson transformation presented through a simple example," *Progress In Electromagnetics Research*, Vol. 75, 137, 2007.
48. Mandilara, A., C. Valagiannopoulos, and V. M. Akulin, "Classical and quantum dispersion-free coherent propagation by tailoring multimodal coupling," *Phys. Rev. A*, Vol. 99, 023849, 2019.
49. Abrashuly, A. and C. Valagiannopoulos, "Limits for absorption and scattering by core-shell nanowires in the visible spectrum," *Phys. Rev. Appl.*, Vol. 11, 014051, 2019.
50. Adachi, S., *Properties of Semiconductor Alloys: Group-IV, III-V and II-VI Semiconductors*, John Wiley & Sons, New York, USA, 2009.
51. Miroshnichenko, A. E., S. Flach, and Y. S. Kivshar, "Fano resonances in nanoscale structures," *Rev. Mod. Phys.*, Vol. 82, 2257, 2010.
52. Valagiannopoulos, C., "Steering of quantum signals along coupled paths of arbitrary curvature," *J. Opt. Soc. Am. B*, Vol. 38, 263, 2021.